Advantages of polarization control in RABBITT

Maria M. Popova and Elena V. Gryzlova
Skobeltsyn Institute of Nuclear Physics, Lomonosov Moscow State University, 119991 Moscow, Russia
and A.V. Gaponov-Grekhov Institute of Applied Physics, Russian Academy of Sciences, 603950 Nizhny Novgorod, Russia

Sergei N. Yudin and Alexei N. Grum-Grzhimailo
Skobeltsyn Institute of Nuclear Physics, Lomonosov Moscow State University, 119991 Moscow, Russia

(Received 29 October 2024; accepted 12 February 2025; published xxxxxxxxxx)

The reconstruction of attosecond beating by interference of two-photon transitions (RABBITT) setup is theoretically studied for various combinations of extreme ultraviolet and infrared (IR) field components polarization: "linear+linear," "linear+circular" with crossed propagation directions, and "circular+circular" with parallel propagation directions. We examine the general properties of photoelectron angular distributions and their response to the variation of the IR pulse delay. Numerical simulations are performed for the neon valence shell ionization into the structureless continuum using two approaches: time-dependent perturbation theory and the solution of amplitude rate equations. To distinguish between "geometrical" governed by fields polarization and spectroscopic features, we provide an additional analysis for the case of s-shell ionization.

DOI: 10.1103/PhysRevA.00.003100

I. INTRODUCTION

Since the very beginning of photoionization experiments, it has been well known that angle-resolved measurements provide more profound and detailed information about a process than measurements of angle-integrated probabilities [1]. The application of a multicolor field significantly enhances experimental capabilities because the polarization and propagation directions of the field components can be modulated separately [2]. This has paved the way for measurements of different types of dichroism, primarily linear and circular magnetic dichroism. The first attempts to access dynamical peculiarities of multiphoton ionization were based on variation of the time offset (lag) between pump and probe fields [3,4]. The development of highly coherent sources of extreme ultraviolet (XUV) and x-ray radiation, such as high-order harmonic generation (HHG) setups [5–7] or x-ray free-electron lasers (XFELs) [8,9], opens a fruitful perspective for vector correlation control in attosecond metrology. That has made possible experimental studying of the dynamics of small quantum systems on attosecond timescales [10–13].

Attosecond metrology based on the RABBITT (reconstruction of attosecond beating by interference of two-photon transitions) scheme [14], where an electron is promoted to the continuum by an XUV harmonic and then additionally absorbs or emits an optical [infrared (IR)] photon, started with angle-integrated experiments [15–18] and corresponding theoretical considerations [19–21]. Meanwhile, the interference of pathways underlying the scheme manifests differently in different waves (s, p, d,...) at different photoemission angles [22]. RABBITT experiments have advanced to the angle-resolved case [23–27], and various theoretical approaches have been employed [28]. Angle-resolved measurements provide more detailed information and allow for the separation different pathways [22,29–34]. Moreover, considering that the energy dependency of vector correlations differs from that of angle-integrated one [35] and may be narrower and shifted, the investigation may be useful for resolving overlapping resonances or in case where the XUV spectrum is very broad, causing single- and two-photon signals to overlap in energy. A separate branch of investigations is devoted to further tuning of the RABBITT technique in solids [36–38], where, in addition, a position of a target itself relative to the polarization of the electromagnetic field should be carefully considered.

The ability to perform angle-resolved measurements is a milestone for schemes with a mixture of waves with different parities in a sideband: (a) XUV harmonics differ by 3ω [39–41], (b) a bichromatic combination ω and 2ω is applied [24], and (c) significant quadrupole effects are expected.

Despite the significant progress made in the field, very few studies involving different harmonics' polarizations (or their directions) are reported [28,30,42,43]. Given the essential progress in the generation of circularly and elliptically polarized harmonics [44–47], there is a need for a systematic investigation of polarization effects in the RABBITT setup. Special attention in such an investigation must be paid to angle-resolved observables. It is important to emphasize that for some combinations polarizations and propagation directions of the components, RABBITT oscillations may appear only in angle-resolved parameters, even in a conventional scheme with XUV components that differ by 2ω.

Unless otherwise specified, the atomic system of units is used.

II. THEORETICAL BASEMENT FOR THE RABBIT DESCRIPTION

In this paper we extend the approaches based on solving an analog of rate equations for the amplitudes and time-dependent perturbation theory applied earlier for linearly

TABLE I. The polarization coefficients c_λ [see Eq. (1)] in the cyclic basis $\{-, 0, +\}$ for different geometries and the list of allowed channels. The index (u) marks the channels proceeding with absorption of the IR photon, (d) with emission.

Geometry system	$\uparrow\rightarrow$ $z\|\|\boldsymbol{E}_{\rm XUV}$	$\uparrow\circlearrowleft$ $z\|\|\boldsymbol{E}_{\rm XUV}$	$\circlearrowleft\uparrow$ $z\|\|\boldsymbol{k}_{\rm XUV}$	$\circlearrowleft\circlearrowleft$ $z\|\|\boldsymbol{k}_{\rm XUV}$
$c_{\rm XUV}$	$\{0, 1, 0\}$	$\{0, 1, 0\}$	$\{0, 0, 1\}$	$\{0, 0, 1\}$
$c_{\rm IR}$	$\{\frac{e^{i\gamma}}{\sqrt{2}}, 0, -\frac{e^{-i\gamma}}{\sqrt{2}}\}$	$\{0, 0, 1\}$	$\{0, 1, 0\}$	$\{0, 0, 1\}$
He-like	$\varepsilon d^{u,d}$	$\varepsilon d^{u,d}$	$\varepsilon d^{u,d}$	$\varepsilon d^{u,d}, \varepsilon s^{d}$ $\varepsilon p^1 S^u$
Noble gases	$\varepsilon p^1 P^{u,d}$ $\varepsilon p^1 D^{u,d}$ $\varepsilon f^1 D^{u,d}$	$\varepsilon p^1 P^{u,d}$ $\varepsilon p^1 D^{u,d}$ $\varepsilon f^1 D^{u,d}$	$\varepsilon p^1 P^{u,d}$ $\varepsilon p^1 D^{u,d}$ $\varepsilon f^1 D^{u,d}$	$\varepsilon p^1 P^{u}$ $\varepsilon p^1 D^{u,d}$ $\varepsilon f^1 D^{u,d}$

polarized fields [48,49] to systems with more complex geometries (polarization and propagation direction of the field component). Thus, here we briefly describe the methods clearly highlighting the polarization aspects.

The electromagnetic field is presented as a sum of XUV harmonics of an order N generated on a seed IR pulse:

$$\boldsymbol{E}(t) = \mathrm{Re}\left[\sum_{N\Lambda\lambda} E_{\rm XUV} c_\Lambda \boldsymbol{\epsilon}_\Lambda e^{-i(N\omega t+\phi_N)} + E_{\rm ir} c_\lambda \boldsymbol{\epsilon}_\lambda e^{-i(\omega t+\phi)}\right], \tag{1}$$

where $E_{\rm XUV} = E^0_{\rm XUV}\cos^2(\frac{t}{\tau})$ and $E_{\rm IR} = E^0_{\rm IR}\cos^2(\frac{2t}{\tau})$ are slowly varying envelopes with $E^0_{\rm IR}$ and $E^0_{\rm XUV}$ being strengths of the IR and XUV components, respectively, and τ determines the pulse duration; ϕ_N is Nth XUV components' phase, and ϕ is the varying phase shift of the IR pulse connected with the IR pulse delay $\tau_{\rm del}$ as $\phi = 2\omega\tau_{\rm del}$. We use a cosine envelope instead of a Gaussian one because it provides smoothness at the (finite) edges of the pulse. The field polarization is determined by a decomposition over cyclic coordinate vectors $\boldsymbol{\epsilon}_{\lambda/\Lambda=1} = -(\boldsymbol{\epsilon}_x - i\boldsymbol{\epsilon}_y)/\sqrt{2}$, $\boldsymbol{\epsilon}_{\lambda/\Lambda=-1} = -(\boldsymbol{\epsilon}_x + i\boldsymbol{\epsilon}_y)/\sqrt{2}$, and $\boldsymbol{\epsilon}_{\lambda/\Lambda=0} = \boldsymbol{\epsilon}_z$ with coefficients $c_{\lambda/\Lambda}$.

If a quantization axis is aligned with the field propagation direction, then the field of arbitrary polarization can be represented as a combination of two waves with right ($\boldsymbol{\epsilon}_{+1}$) and left ($\boldsymbol{\epsilon}_{-1}$) circular polarization. Since the propagation direction may not coincide with the quantization axis z, nonzero contribution of $\boldsymbol{\epsilon}_{\lambda/\Lambda=0}$ appears (see Table I and Fig. 1).

The cyclic basis is convenient because of its direct connection with selection rules for the magnetic quantum number M in systems with spherical symmetry. For example, the absorption of a photon with helicity $\lambda = +1$ transfers a state with magnetic quantum number M into one with $M + 1$ (see Fig. 2).

The atomic Hamiltonian is presented in the form

$$i\frac{\partial}{\partial t}\Psi(\boldsymbol{r}, t) = (\hat{H}_{\rm at} + \hat{H}_{\rm int}(t))\Psi(\boldsymbol{r}, t), \tag{2}$$

where $\hat{H}_{\rm at}$ is unperturbed Hamiltonian and $\hat{H}_{\rm int}(t)$ describes the interaction with electromagnetic field in the dipole approximation and velocity gauge with electric field potential $\boldsymbol{A}(t) = -c\int \boldsymbol{E}(t)dt$.

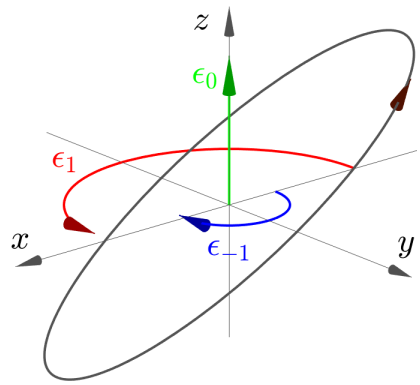

FIG. 1. An example of decomposition of an electric field with ellipticity equal to 0.4 and an angle between major ellipse axis and its projection to xy plane equal to $-\pi/6$ over cyclic coordinate vectors in a chosen coordinate system.

We adopt the LS-coupling scheme, which is good for describing the ionization of noble gases up to Kr in featureless continuum, as relativistic effects do not play a major role. In the LS-coupling scheme within the frozen core approximation, eigenfunctions of the system $\psi_{\alpha_n}(\varepsilon_n, \boldsymbol{r})$ depend on the following quantum numbers: energy ε_n (ε without an index if a state belongs to a continuum spectrum), core (ion) orbital momentum, and spin L_c and S_c, active electron angular momentum l and spin $s = \frac{1}{2}$, total angular momentum L and spin S, and their projections $M_L = M$ and M_S. Accounting that the electric dipole operator does not change spin $\Delta S = 0$ and an atom is initially in a state with a definite spin, we can rule out the spin quantum numbers for brevity: $\psi_{\alpha_n}(\varepsilon_n, \boldsymbol{r}) \equiv \psi_{(L_c l)L(S_c\frac{1}{2})SM_LM_S}(\varepsilon_n, \boldsymbol{r}) \equiv \psi_{(L_c l)LM}(\varepsilon_n, \boldsymbol{r})$. A wave function of the system $\Psi(\boldsymbol{r}, t)$ is expanded in the basis of eigenfunctions of the unperturbed Hamiltonian:

$$\hat{H}_{\rm at}\psi_{\alpha_n}(\varepsilon_n, \boldsymbol{r}) = \varepsilon_n\psi_{\alpha_n}(\varepsilon_n, \boldsymbol{r}), \tag{3}$$

$$\Psi(\boldsymbol{r}, t) = \sum_{L_c lLM}\left(\sum_n \mathcal{U}_{(L_c l)LM}(\varepsilon_n, t)\psi_{\alpha_n}(\varepsilon_n, \boldsymbol{r})e^{-i\varepsilon_n t} + \int d\varepsilon\, \mathcal{U}_{(L_c l)LM}(\varepsilon, t)\psi_{\alpha_\varepsilon}(\varepsilon, \boldsymbol{r})e^{-i\varepsilon t}\right), \tag{4}$$

where α_ε means a set of quantum numbers of a state with an electron in continuum.

Then the system of differential equations for expansion coefficients

$$\frac{d\mathcal{U}_{(L_c l)LM}(\varepsilon_{n'}, t)}{dt} = -i\sum_n e^{i(\varepsilon_{n'}-\varepsilon_n)t}\langle\psi_{\alpha'_n}|\hat{H}_{\rm int}(t)|\psi_{\alpha_n}\rangle \times \mathcal{U}_{(L_c l)LM}(\varepsilon_n, t) \tag{5}$$

is solved numerically in the *amplitude coefficient equations (ACE)* method [50]. To describe the continuum states in (5), the continuum discretization was applied, i.e., integration was replaced by summation with uniform energy step $d\varepsilon$. Thereby, $|\mathcal{U}_{(L_c l)LM}(\varepsilon_\epsilon, t)|^2$ is the probability of finding an electron within a neighborhood $d\epsilon$ of the energy ε at time t.

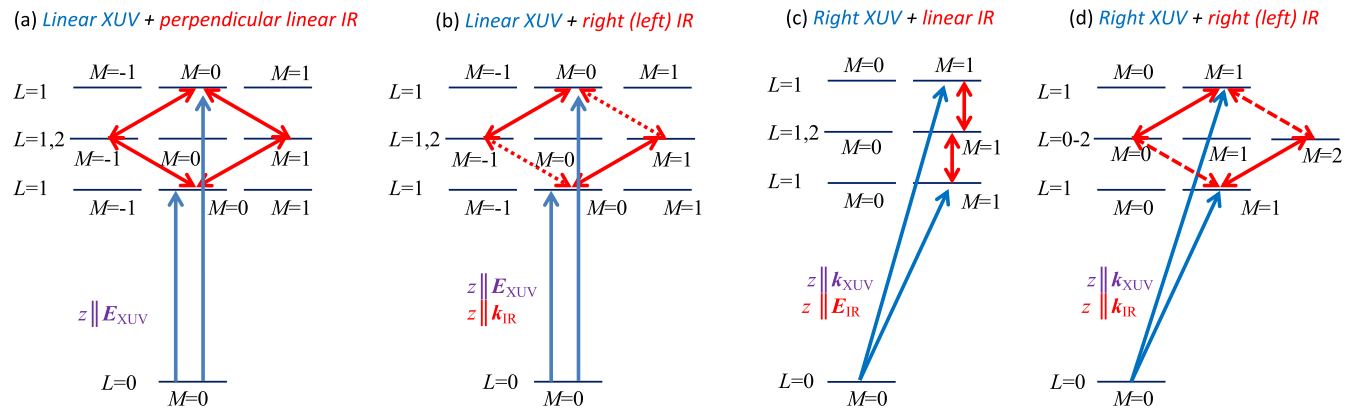

FIG. 2. The scheme of RABBITT for different geometries: (a) the XUV comb and IR field are linearly polarized in the orthogonal directions; (b) linearly polarized XUV comb and circularly polarized IR; (c) circularly polarized XUV comb and linearly polarized IR field; (d) both XUV comb and IR field are circularly polarized.

The vector potential can be further decomposed into $A_{\rm XUV}(t)$ that describes the XUV comb and $A^u_{\rm IR}(t)$ and $A^d_{\rm IR}(t)$ that describe the IR and behave as $e^{-i(\omega t+\phi)}$ and $e^{i(\omega t+\phi)}$, respectively. The component $A^u_{\rm IR}(t)$ is associated with the absorption of an IR photon (photoelectron goes "up" in energy), and $A^d_{\rm IR}(t)$ with the emission (photoelectron goes "down" in energy).

Within the framework of *perturbation theory* (PT), the coefficients $\mathcal{U}_{(L_c l)LM}(\varepsilon_n, t)$ in Eq. (5) are, in turn, expanded into a series.

Henceforth, we specify a target as a shell of an unpolarized atom with an initial orbital angular momentum $L = 0$.

The first-order coefficients describe direct ionization to the main photolines (ML) by XUV components of the electric field:

$$\mathcal{U}^{(1)}_{(L_c l)LM}(\varepsilon_f, t) = c_\Lambda \frac{1}{\sqrt{3}}(00, 1\Lambda \mid 1M) D^{(1)}_{(L_c l)1}, \tag{6}$$

$$D^{(1)}_{(L_c l)1} = -i\langle \varepsilon_f; (L_c l)1 \,||\, \hat{D} \,||\, \varepsilon_0, 0\rangle \int_{-\tau/2}^{\tau/2} A_{\rm xuv}(t) e^{i(\varepsilon_f-\varepsilon_0)t} dt, \tag{7}$$

where $(00, 1\Lambda \mid 1M)$ is equal to 1 for each Λ and it determines a specific M. We suppose the component to be either circularly or linearly polarized that means that with appropriate choice of a coordinate system only one $c_\Lambda \neq 0$.

The second-order amplitudes describe absorption ("u") or emission ("d") of an IR photon leading to appearance of sidebands (SB) by up- and down-energy transitions:

$$\mathcal{U}^{(2),u/d}_{(L_c l)LM}(\varepsilon_f, t) = \frac{(\pm 1)^\lambda}{\sqrt{3}\hat{L}} \sum_\lambda c_\lambda (1\Lambda, 1\pm\lambda \mid LM) D^{(2),u/d}_{(L_c l)L}, \tag{8}$$

$$D^{(2),u/d}_{(L_c l)L} = \sum\!\!\!\!\!\!\int_n \langle \varepsilon_f, (L_c l)L \,||\, D \,||\, \varepsilon_n, 1\rangle \langle \varepsilon_n, 1 \,||\, D \,||\, \varepsilon_0, 0\rangle \times \int_{-\tau}^{\tau} A^{u/d}_{\rm IR}(t) e^{i(\varepsilon_f-\varepsilon_n)t} \int_{-\tau/2}^{t} A_{\rm xuv}(t') e^{i(\varepsilon_n-\varepsilon_0)t'} dt' dt, \tag{9}$$

where the plus (+) sign is for absorption amplitude, and the minus (−) sign is for emission. Factor $(\pm 1)^\lambda$ comes from taking complex conjugation in cyclic basis: $\epsilon^*_{+1} = -\epsilon_{-1}$ and vice versa. In Eq. (8), conventional notation for Clebsch-Gordan coefficients is used and $\hat{a} = \sqrt{2a+1}$.

The photoelectron angular distribution (PAD) in PT and ACE is described as

$$W(\varepsilon_f, t; \vartheta, \varphi) = \frac{1}{4\pi} \sum_{\substack{kqll'LL' \\ nn'\nu\nu'}} (-1)^{L_c+L+L'+k-M'} \hat{l}\hat{l}'\hat{L}\hat{L}' \times (l0, l'0 \mid k0)(LM, L'-M' \mid kq) \begin{Bmatrix} l & L & L_c \\ L' & l' & k \end{Bmatrix} \times \mathcal{U}^{(n),\nu}_{(L_c l)LM}(\varepsilon_f, t) \mathcal{U}^{(n'),\nu'*}_{(L_c l')L'M'}(\varepsilon_f, t) \frac{\sqrt{4\pi}}{\hat{k}} Y_{kq}(\theta, \varphi), \tag{10}$$

where ν is an order of amplitude in PT (in ACE the resulting amplitude $\mathcal{U}_{(L_c l)LM}(\varepsilon_f, t)$ is an "infinite sum" over ν). In Eq. (10), conventional notations for the Wigner $6j$ symbol and spherical harmonics are used.

In Eq. (10), the terms corresponding to the absorption ($\mathcal{U}^{(2),u}\mathcal{U}^{(2),u*}$) and emission ($\mathcal{U}^{(2),d}\mathcal{U}^{(2),d*}$) of an IR photon do not depend on the IR time delay; the interference term between absorption and emission amplitudes ($\mathcal{U}^{(2),u}\mathcal{U}^{(2),d*}$) depends on the IR delay and oscillates at the double IR frequency 2ω.

III. THE PAD FOR DIFFERENT GEOMETRIES

In Fig. 2, there are schemes of RABBITT spectroscopy for the systems under consideration:

(a) The XUV comb and IR field are linearly polarized in the orthogonal directions (quantization axis is along the XUV component polarization $z \parallel \boldsymbol{E}_{\rm XUV}$), further referred as ↑→.

(b) Linearly polarized XUV comb and circularly polarized IR field (quantization axis is along the XUV component polarization $z \parallel \boldsymbol{E}_{\rm XUV}$ and $\boldsymbol{E}_{\rm XUV} \parallel \boldsymbol{k}_{\rm IR}$), further referred as ↑⟳.

(c) Circularly polarized XUV comb and linearly polarized IR field (quantization axis is along the IR component polarization $z \parallel \boldsymbol{E}_{\rm IR}$ and $\boldsymbol{E}_{\rm IR} \parallel \boldsymbol{k}_{\rm XUV}$), further referred as ⟳↑.

(d) Both the XUV comb and IR field are circularly polarized (quantization axis is along the field propagation direction $z \parallel \boldsymbol{k}_{\rm IR} \parallel \boldsymbol{k}_{\rm XUV}$), further referred as $\circlearrowleft\circlearrowleft$.

These geometries were chosen for possessing the electric field of the highest symmetry. The case of the linearly polarized in the same direction XUV and IR fields was studied by the same methods earlier in [49]. The quantum numbers in Fig. 2 are depicted for a system with initial orbital momentum $L = 0$ (a noble gas). Further, we apply the approach to valence shell ionization of neon and specify the general equations for the s-shell ionization (1s of He, 2s of Ne, 3s of Ar, etc).

In Table I, channels allowed for the different geometries under consideration are presented. For the geometries $\uparrow\rightarrow$, $\circlearrowleft\uparrow$, and $\uparrow\circlearrowleft$ final projection of magnetic quantum number $M = 1$, therefore, the terms are $P\,(L = 1)$ and $D\,(L = 2)$. For the heliumlike systems $l = L$, there is a single d-wave channel because the parity conservation rule prohibits emission of the p wave. The $\circlearrowleft\circlearrowleft$ geometry is exceptional because the S ($L = 0$) (for neon) and εs (for helium) channel is involved for down-energy (equal helicities of IR and XUV) or up-energy (opposite helicities) transitions.

A. A shell of a noble gas

It is convenient to extract a fields' polarization-independent dynamical parameter $B_k^{(\nu\mu)}[L, L']$ from the general angular distribution equation (10). For the sidebands in the second order of PT it takes a form

$$B_k^{(\mu\mu')}[L, L'] = \frac{(-1)^{L_f+L+L'}}{12\pi} \sum_{ll'} \hat{l}\hat{l}'(l0, l'0 \,|\, k0) \times \begin{Bmatrix} L & L' & k \\ l' & l & L_f \end{Bmatrix} D^{(2),\mu}_{(L_c l)L} D^{(2),\mu'*}_{(L_c l)L}, \quad (11)$$

where $\mu, \mu' = u, d$, and the dynamical parameters obey permutation equation $B_k^{(\mu\mu')}[L, L'] = B_k^{(\mu'\mu)}[L', L]^*$. In the case of the ACE, the definition (11) is fair, except that instead of the second-order term $D^{(2),\mu}_{(L_c l)L}$ one must consider a complete amplitude that possesses given quantum numbers.

With the help of Eq. (11) the angular distributions for specific geometries can be written in an easier for an analysis form as $B_k^{(\nu\mu)}[L, L']$s do not depend on polarization and are the same for every geometry:

$$W^{\uparrow\rightarrow}(\theta,\varphi) = \sum_{kLL'} \frac{(-1)^{L+L'+1}}{2} \big(B_k^{(dd)}[L, L'] + B_k^{(uu)}[L, L'] + B_k^{(ud)}[L, L'] + B_k^{(du)}[L, L']\big) \times \left((L1, L'-1 \,|\, k0)P_k(\cos\theta) + (-1)^{L'}(L1, L'1 \,|\, k2)\frac{\sqrt{4\pi}}{\hat{k}}[\eta Y_{k2}(\theta,\varphi) + \eta^* Y_{k-2}(\theta,\varphi)]\right) \quad (12)$$

$$= \frac{\sigma^{\uparrow\rightarrow}}{4\pi}\left(1 + \sum_{k=2,4} \beta_k^{\uparrow\rightarrow} P_k(\cos\theta) + \beta_{k2}^{\uparrow\rightarrow}\frac{\sqrt{4\pi}}{\hat{k}}[\eta Y_{k2}(\theta,\varphi) + \eta^* Y_{k-2}(\theta,\varphi)]\right); \quad (13)$$

$$W^{\uparrow\circlearrowleft}(\theta,\varphi) = \sum_{kLL'} \frac{(-1)^{L+L'+1}}{2}(L1, L'-1 \,|\, k0)\big(B_k^{(dd)}[L, L'] + B_k^{(uu)}[L, L']\big)P_k(\cos\theta) \quad (14)$$

$$+ (L1, L'1 \,|\, k2)\frac{(-1)^L}{2}\frac{\sqrt{4\pi}}{\hat{k}}\big[B_k^{(ud)}[L, L']Y_{k2}(\theta,\varphi) + B_k^{(du)}[L', L]Y_{k-2}(\theta,\varphi)\big]$$

$$= \frac{\sigma^{\uparrow\circlearrowleft}}{4\pi}\left(1 + \sum_{k=2.4} \beta_k^{\uparrow\circlearrowleft} P_k(\cos\theta) + \frac{\sqrt{4\pi}}{\hat{k}}(\beta_{k2}^{\uparrow\circlearrowleft} Y_{k2}(\theta,\varphi) + \beta_{k2}^{\uparrow\circlearrowleft *} Y_{k-2}(\theta,\varphi))\right); \quad (15)$$

$$W^{\circlearrowleft\uparrow}(\theta,\varphi) = \sum_{kLL'} (L1, L'-1 \,|\, k0)\frac{-1}{2}\big(B_k^{(dd)}[L, L'] + B_k^{(uu)}[L, L'] + B_k^{(ud)}[L, L'] + B_k^{(du)}[L', L]\big)P_k(\cos\theta) \quad (16)$$

$$= \frac{\sigma^{\circlearrowleft\uparrow}}{4\pi}\left(1 + \sum_{k=2,4} \beta_k^{\circlearrowleft\uparrow} P_k(\cos\theta)\right); \quad (17)$$

$$W^{\circlearrowleft\circlearrowleft}(\theta,\varphi) = \sum_{kLL'} \big[(L0, L'0 \,|\, k0)(11, 1-1 \,|\, L0)(11, 1-1 \,|\, L'0)B_k^{(dd)}[L, L'] + (22, 2-2 \,|\, k0)B_k^{(uu)}[2, 2]\big]P_k(\cos\theta)$$

$$- (22, L'0 \,|\, k2)(11, 1-1 \,|\, L'0)\frac{\sqrt{4\pi}}{\hat{k}}\big[B_k^{(ud)}[2, L']Y_{k2}(\theta,\varphi) + B_k^{(du)}[L', 2]Y_{k-2}(\theta,\varphi)\big] \quad (18)$$

$$= \frac{\sigma^{\circlearrowleft\circlearrowleft}}{4\pi}\left(1 + \sum_{k=2.4} \beta_k^{\circlearrowleft\circlearrowleft} P_k(\cos\theta) + \frac{\sqrt{4\pi}}{\hat{k}}[\beta_{k2}^{\circlearrowleft\circlearrowleft} Y_{k2}(\theta,\varphi) + \beta_{k2}^{\circlearrowleft\circlearrowleft *} Y_{k-2}(\theta,\varphi)]\right). \quad (19)$$

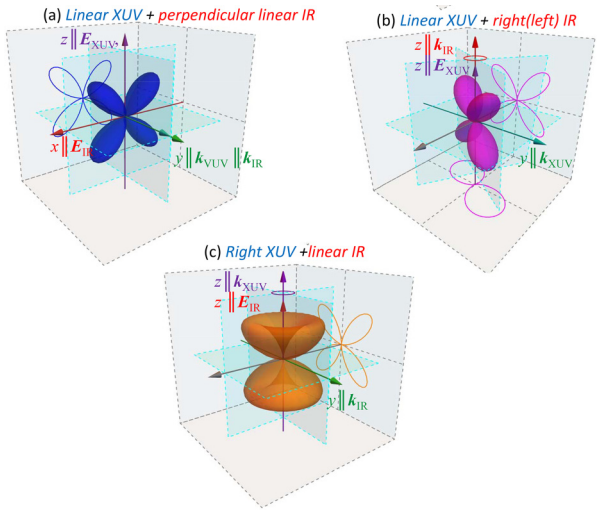

FIG. 3. The sample of PAD for the case of heliumlike system and different geometries.

The parameter $\eta = -\exp[-2i\gamma]/2$ is defined by the angle γ of IR polarization vector with respect to the x axis in the xy plane. Equations (13), (15), (17), and (19) themselves are the definition of the integral photoemission probabilities (a probability of photoelectron emission per atom during a pulse, later referred as "electron spectrum") $\sigma^{\cdots}$'s ($k = 0$) and angular anisotropy parameters $\beta_{kq}^{\cdots}$'s that allow us to characterize the shape of angular distributions by a few numbers since they are factors in front of the corresponding Legendre polynomials or spherical harmonics (see Fig. 4). The parameters $\beta_{22(42)}$ are defined to be in consistency with conventional parameters $\beta_{2(4)}$ [$\frac{\sqrt{4\pi}}{\hat{k}} Y_{k0}(\theta, \varphi)$ is a Legendre polynomial $P_k(\cos\theta)$].

The following general conclusions can be drawn about the properties of the angle-integrated probabilities and PADs:

(1) For the $\uparrow\rightarrow$ and $\circlearrowleft\uparrow$ geometries, the IR phase ϕ affects both the overall probability for an electron to be emitted at a given energy [$\sigma = \sigma(\phi)$] and the angular anisotropy parameters [$\beta = \beta(\phi)$]; all of the angular anisotropy parameters are real; PAD inherits the symmetries of the resulting field: for the case $\uparrow\rightarrow$, there are three orthogonal symmetry planes [see Fig. 3(a)] and for the case $\circlearrowleft\uparrow$, there is axial symmetry with respect to the IR polarization vector accompanied with orthogonal symmetry plane [see Fig. 3(c)].

(2) For the $\uparrow\circlearrowleft$ and $\circlearrowleft\circlearrowleft$ geometries, the phase-averaged part of Eqs. (14) and (18) which contains B^{dd} and B^{uu} is axially symmetrical, while the interference term contains B^{ud} and B^{du} that depend on azimuth angle φ; as a result, a complete PAD possesses the only one symmetry plane orthogonal to the IR propagation direction. Neither angle-averaged spectrum nor the PAD changes with variation of the IR phase ϕ except for the rotation of the last around z axis: Eqs. (15) and (19) incorporating $\beta_{22,42}$ depend on IR phase as $\exp[\pm 2i(\phi - \varphi)]$. The angular anisotropy parameters $\beta_{2(4),2}$ caused by interference are complex.

(3) The circular magnetic dichroism can be observed only for the $\circlearrowleft\circlearrowleft$ geometry.

(4) The angular anisotropy parameters being a ratio of harmonic functions of ϕ are periodical but not harmonic functions of IR phase ϕ.

B. Heliumlike system

In this paragraph we consider additional features which arise when the ionized shell is an s shell, so-called *heliumlike system*. In this case, the number of allowed ionization channels reduces significantly and they are characterized only by photoelectron angular momentum l. For $\uparrow\rightarrow$, $\uparrow\circlearrowleft$, and $\circlearrowleft\uparrow$ geometries, there is only one allowed channel: ionization to d wave, for $\circlearrowleft\circlearrowleft$ geometry, there are two channels: d and s waves (see Table I). Equation (10) for the sidebands turns into an extremely simple form

$$W^{\uparrow\rightarrow}(\theta,\varphi) = \frac{1}{8\pi}\left(\left|D^u_{\varepsilon d}\right|^2 + \left|D^d_{\varepsilon d}\right|^2 + D^u_{\varepsilon d}D^{d*}_{\varepsilon d} + D^d_{\varepsilon d}D^{u*}_{\varepsilon d}\right) \times \sin^2\theta\,\cos^2\theta\,\cos^2(\varphi - \phi - \gamma), \tag{20}$$

$$W^{\uparrow\circlearrowleft}(\theta,\varphi) = \frac{1}{16\pi}\left(\left|D^u_{\varepsilon d}\right|^2 + \left|D^d_{\varepsilon d}\right|^2 + e^{2i\varphi}D^u_{\varepsilon d}D^{d*}_{\varepsilon d} + e^{-2i\varphi}D^d_{\varepsilon d}D^{u*}_{\varepsilon d}\right)\cos^2\theta\,\sin^2\theta, \tag{21}$$

$$W^{\circlearrowleft\uparrow}(\theta,\varphi) = \frac{1}{16\pi}\left(\left|D^u_{\varepsilon d}\right|^2 + \left|D^d_{\varepsilon d}\right|^2 + D^u_{\varepsilon d}D^{d*}_{\varepsilon d} + D^d_{\varepsilon d}D^{u*}_{\varepsilon d}\right) \times \cos^2\theta\,\sin^2\theta\,, \tag{22}$$

$$\begin{aligned} W^{\circlearrowleft\circlearrowleft}(\theta,\varphi) = {} & \frac{1}{12\pi}\sum_{kll'}(l0, l'0\,|\,k0)^2(11, 1-1\,|\,l0) \\ & \times (11, 1-1\,|\,l'0)D^d_{\varepsilon l}D^{d*}_{\varepsilon l'}P_k(\cos\theta) \\ & + \frac{1}{32\pi}|D^u_{\varepsilon d}|^2\sin^4\theta - \frac{1}{12\pi}\sum_{kl'}(20, l'0\,|\,k0) \\ & \times (22, l'0\,|\,k2)(11, 1-1\,|\,l'0)\frac{\sqrt{4\pi}}{\hat{k}} \\ & \times \left[D^u_{\varepsilon d}D^{d*}_{\varepsilon l'}Y_{k2}(\theta,\varphi) + D^{d*}_{\varepsilon d}D^d_{\varepsilon l'}Y_{k-2}(\theta,\varphi)\right]. \end{aligned} \tag{23}$$

Here $D^{u/d}_{\varepsilon l} \equiv D^{(2),u/d}_{(0l)l}$. In Fig. 3, the general pattern of PAD for heliumlike system is presented. For the $\uparrow\rightarrow$ and $\circlearrowleft\uparrow$ geometries they are unconditional, for $\uparrow\circlearrowleft$ plotted under assumption that $D^u_{\varepsilon d} = D^d_{\varepsilon d}$.

In the case of heliumlike system one may conclude the following:

(1) For the $\uparrow\rightarrow$ and $\circlearrowleft\uparrow$ geometries, only d wave left, and absorption and emission amplitudes come into the equations equally. The PADs turn into completely geometrical form with $\beta_2^{\uparrow\rightarrow,\circlearrowleft\uparrow} = \frac{5}{7}$, $\beta_4^{\uparrow\rightarrow,\circlearrowleft\uparrow} = -\frac{12}{7}$, $\beta_{22}^{\uparrow\rightarrow} = -5\sqrt{6}/7$, and $\beta_{42}^{\uparrow\rightarrow} = -6\sqrt{10}/7$.

(2) For the $\uparrow\circlearrowleft$ geometry, d-wave absorption (u) and emission (d) amplitudes contribute to PAD differently, and the PAD is partly geometrical: $\beta_2^{\uparrow\circlearrowleft} = \frac{5}{7}$, $\beta_4^{\uparrow\circlearrowleft} = -\frac{12}{7}$:

$$\beta_{22}^{\uparrow\circlearrowleft} = \frac{5\sqrt{6}D^u_{\varepsilon d}D^{d*}_{\varepsilon d}}{7\left(\left|D^u_{\varepsilon d}\right|^2 + \left|D^d_{\varepsilon d}\right|^2\right)}, \quad \beta_{42}^{\uparrow\circlearrowleft} = \frac{6\sqrt{10}D^u_{\varepsilon d}D^{d*}_{\varepsilon d}}{7\left(\left|D^u_{\varepsilon d}\right|^2 + \left|D^d_{\varepsilon d}\right|^2\right)}.$$

(3) For $\uparrow\rightarrow$–$\circlearrowleft\uparrow$ geometries, the maximal probability of electron emission is observed at the polar angle $\theta = \pi/4$.

(4) For $\circlearrowleft\uparrow$ and $\circlearrowleft\circlearrowleft$ geometries, the PADs possess the same symmetries as in the general case. For $\uparrow\rightarrow$ and $\uparrow\circlearrowleft$ geometries, two additional symmetry planes arise: for $\uparrow\rightarrow$

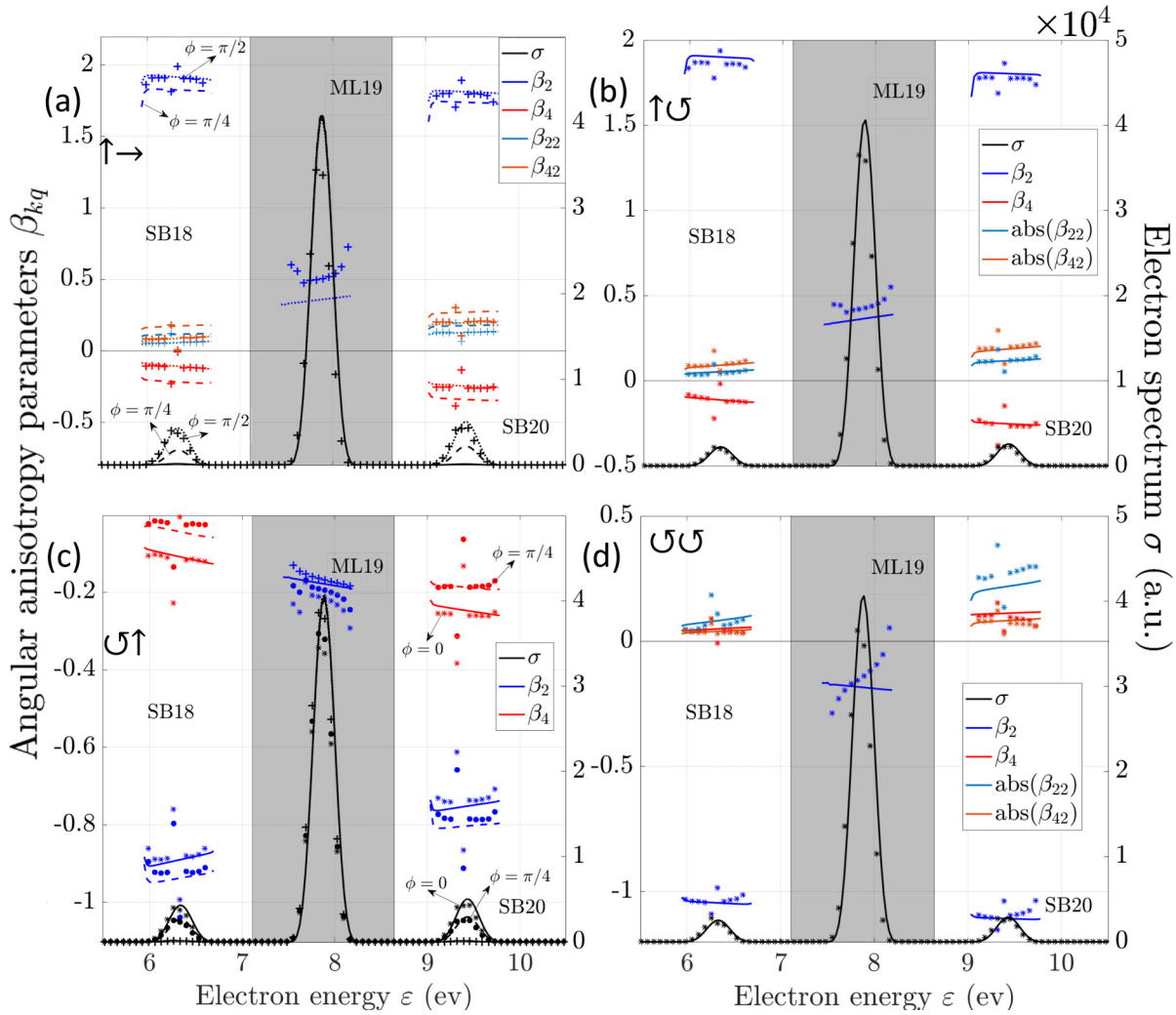

FIG. 4. Electron spectra σ (in atomic units) and angular anisotropy parameters β_{kq} as defined in Eqs. (12)–(18). Colors indicate a specific parameter (see the legends), and line type: IR phase and a model (solid lines are for PT and $\phi = 0$, stars are for ACE and $\phi = 0$; dashed lines and circles are for PT and ACE for $\phi = \pi/4$, respectively; dotted lines and crosses are for PT and ACE for $\phi = \pi/2$). Parameters of the electric field (1) are $\omega = 1.55$ eV with its 17th, 19th, and 21nd harmonics; $E^0_{\rm XUV} = 10^{-4}$ a.u., $E^0_{\rm IR} = 2.5 \times 10^{-3}$ a.u., and $\tau = 10$ fs.

they are defined by the geometry and make angle $\pm\pi/4$ with polarization vectors of IR and XUV comb; for $\uparrow\circlearrowleft$ they are defined by phase between up and down pathways and make an angle with x axis equal to $\mathrm{Arg}[D^u_{\varepsilon d} D^{d*}_{\varepsilon d}]$.

(5) For the $\circlearrowleft\circlearrowleft$ geometry, there is a difference between pathways with the absorption and emission of an IR photon. While the first one leads to d wave only, the second allows also s wave. Therefore, the absorption pathway contributes to the plane orthogonal to the fields' propagation direction, and the emission pathway may contribute in the fields' propagation direction.

IV. NUMERICAL EXAMPLE AND DISCUSSION

In this section, the results of calculations of photoionization probability and angular anisotropy parameters in the neon valance shell induced by a pulse composed of an IR field with $\omega = 1.55$ eV and its 17th, 19th, and 21nd harmonics are presented. The electric field parameters were set to the values typical for RABBITT experiments: $E^0_{\rm XUV} = 10^{-4}$ a.u., $E^0_{\rm IR} = 2.5 \times 10^{-3}$ a.u., and $\tau = 10$ fs. Note that according to Eq. (1), the duration of XUV components is half that of the IR component.

Reduced dipole matrix elements between the ground state $2s^2 2p^6\, {}^1S$ and continuum states $2s^2 2p^5 \varepsilon l\, {}^1L$ in Eq. (7) were calculated in the MCHF package [51] with a nonorthogonal $2p$ orbital. For the ground state, the experimental ionization energy was used. Reduced dipole matrix elements between continuum states in Eq. (9) were calculated using a method described in [52] involving angular momentum algebra [48] to convert the radial integrals into the matrix elements in an appropriate angular momentum coupling scheme.

For the ACE method, $d\varepsilon$ was chosen to be 2.5×10^{-3} a.u. within the energy range $(0, \div 0.625)$ a.u. The numerical results are stable over a broad diapason of range and step parameters for intensities typical for RABBITT experiments (10^{11}–10^{13} W/cm^2). To achieve convergence in the angle-differential parameters, the energy range must be at least one IR photon energy beyond the one under consideration; the step size must be sufficiently fine such that the sideband includes

at least five data points: two spikes appear in the differential parameters (see Fig. 4) near the sideband cross-section maxima, yielding unreliable values; these points converge as the step size reduces.

In Fig. 4, dimensionless parameters β_{kq} defined by Eqs. (12)–(19) calculated by both ACE and PT methods are plotted alongside the integrated spectrum. Here, all ϕ_N were set to zero. The central peak is a mainline caused by 19th harmonic absorbtion, two lower peaks on either side of ML19 are the sidebands SB18 and SB20. For ↑→ and ↻↑ geometries, calculations at three IR component phases $\phi = 0,\ \pi/4$, and $\pi/2$ of are presented. For ↑↻ and ↻↻ geometries, the presented parameters do not depend on IR phase. For the ↑→ geometry at $\phi = 0$ and the ↻↑ geometry at $\phi = \pi/2$, the integrated probability in sidebands is negligible, therefore, dimensionless anisotropy parameters are become less reliable and are not presented. The agreement between the methods is generally good. Given that the ACE calculation is more rugged, it is shown selectively where it is relevant to the discussion, so as not to compromise overall readability.

The angular anisotropy parameters vary smoothly across the peaks except the edges where photoemission probability drops down. As it is clear from Eqs. (15) and (19), $\beta_{22(42)}$ determine the PADs' dependency on the azimuth angle φ, while $\beta_{2(4)}$ determine the axially symmetrical contribution. In all cases, the parameters β_{22} are considerably smaller than β_2 and comparable to β_4 and β_{42}. The small magnitude of these parameters is a result of interference between ionization to f and p waves.

If only f wave is important due to a spectroscopic feature, for the geometries ↑→–'↻↑ the anisotropy parameters tend to $\beta_2 \to \frac{4}{7}$, $\beta_4 \to -\frac{4}{7}$, $\beta_{22} \to -2\sqrt{6}/7$, and $\beta_{42} \to -\sqrt{10}/7$.

As previously mentioned, in the ↑→ and ↻↑ geometries, both the spectrum and parameters β_{kq} depend on the IR phase ϕ [see Figs. 4(a) and 4(c)]. For the ↑→ and ↻↑ geometries, the formal equations for the integrated spectrum and β_4, expressed in terms of the dynamical parameters (11), are identical. Nevertheless, it is important to consider that the corresponding amplitudes depend on the IR phase, and the last, when written in the form of Eq. (1), has a different physical meaning for different geometries. The easiest way to illustrate is that $\phi = 0$ means $\boldsymbol{E}_{\rm XUV} \parallel z$ and $\boldsymbol{E}_{\rm IR} \parallel x$ for ↑→ geometry, while $\phi = 0$ means $\boldsymbol{E}_{\rm XUV} \parallel x$ and $\boldsymbol{E}_{\rm IR} \parallel y$ for ↻↑ geometry. Therefore, the same values of observables are reached at different phases, for example, $\sigma^{\uparrow\rightarrow}(\pi/2) = \sigma^{\circlearrowleft\uparrow}(0)$. The difference in β_2 originates from different signs before the interference terms $B^{\nu\mu}[1,2]$ [see factor $(-1)^{L+L'+1}$ in Eq. (12)]. If for some reason either $L = 1$ (P term) or $L = 2$ (D term) dominates, β_2 in these geometries would also coincide.

In Fig. 5, PADs for different geometries and IR phases are constructed with the data from Fig. 4 for the sideband SB20 at ≈9.5 eV. In the schemes ↑→ and ↑↻, β_2 is positive, therefore, the maximum photoelectron emission is observed along the quantization axis ($\theta = 0, \pi$) because the other β's are much smaller. Earlier it was shown that β_2 is also positive when both of the field components are linearly polarized in the same direction [25,49]. In the schemes ↻↑ and ↻↻, β_2 is negative, therefore, the maximum photoelectron emission is observed in the plane perpendicular to the quantization axis

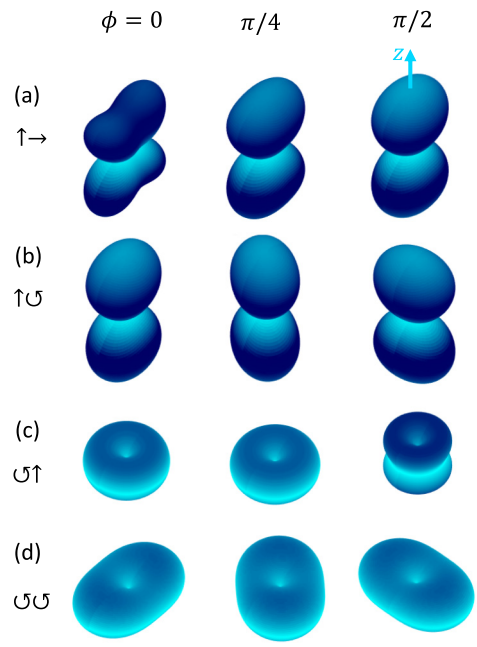

FIG. 5. PADs as defined in Eqs. (12)–(19) for the sideband SB20 at ≈9.5 eV for considered geometries normalized to $\sigma = 1$ for IR field phase $\phi = 0, \pi/4, \pi/2$.

($\theta = \pi/2$). The PADs keep their form for the phases corresponding to substantial signals in the sidebands and diverge for the phases corresponding to minor sidebands ($\phi = 0$ for ↑→ and $\phi = \pi/2$ for ↻↑ geometries): as β_2 sharply changes, the contributions from the term with $Y_{4,22,42}(\theta,\varphi)$ become more significant [see Figs. 5(a) and 5(c)]. For these phases, the PADs resemble the ones for heliumlike case [Figs. 3(a) and 3(c)]. In schemes ↑↻ and ↻↻, as previously mentioned, the PAD rotates around z axis, with the variation of the IR component phase ϕ. For neon, the effect of rotation is more prominent for the geometry ↻↻ [see Figs. 5(b) and 5(d)].

A short comment should be given about *circular dichroism* in the scheme ↻↻. In this geometry, there is an essential difference in the allowed channels for the case when IR and XUV components have the same helicity compared to when they have opposite helicity. In the first case, pathways with IR absorption lead to $L = 2$ (εd for helium), while those with emission lead to $L = 0, 1, 2$ [$\varepsilon s(\varepsilon d)$ for helium)]. In the second case, the situation is opposite. One can easily cast the equation for dichroism using (18) and (23). The interesting feature is that contribution of fourth-rank terms is strictly canceled in the dichroism for any target.

It could be important for experimenters because extraction of higher-rank anisotropy parameters are usually more difficult than those of 2nd rank. Nevertheless, for the region of smooth continuum, the difference in probabilities of up and down channels is little, and dichroism is not significant. One should look for a system with a sharp spectroscopic feature (autoionizing resonance) to observe the circular magnetic dichroism in such a setup.

Until now, we assumed that the phases of all of the XUV harmonics were zero, $\phi_N = 0$. In order to investigate the role of the XUV phases, we chose ↻↑ geometry and assigned several different values to ϕ_{19} (see Fig. 6). One can see that

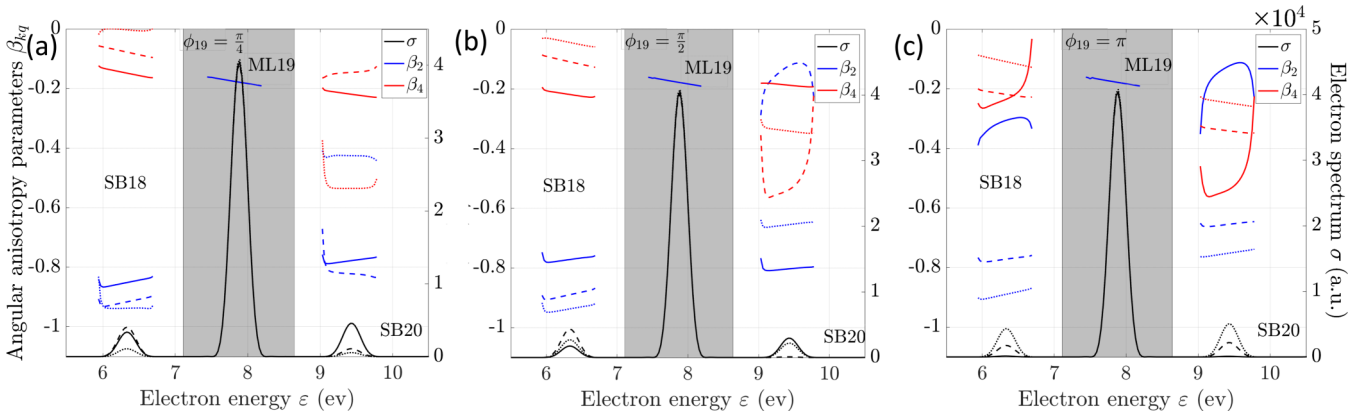

FIG. 6. PT calculations for geometry ↺↑ for different phases of 19th harmonic: $\omega = 1.55$ eV with its 17th, 19th, and 21nd harmonics; $E^0_{\rm XUV} = 10^{-4}$ a.u., $E^0_{\rm IR} = 2.5 \times 10^{-3}$ a.u., $\tau = 10$ fs, $\phi_{19} = \pi/4$ (a), $\pi/2$ (b), and π (c) [see Eq. (1)]. Solid lines are for $\phi = 0$, dashed lines for $\phi = \pi/4$, and dotted lines for $\phi = \pi/2$.

varying the phase of an XUV component leads to a redistribution of the photoemission signal, therefore, the same magnitudes are achieved at different IR phases. The range of variation for the anisotropy parameters remains unchanged.

V. CONCLUSIONS

In this paper, we investigated how the polarization and propagation direction of the field components affect the kinematics of photoionization in the RABBITT scheme. We considered the following scenarios: (a) crossed linearly polarized IR and XUV harmonics; (b), (c) either the XUV comb or the IR field is linearly polarized and the remaining component is circularly polarized and propagating along the linear polarization vector; (d) both the IR and XUV fields are circularly polarized.

Among the considered geometries, setup (c) with circularly polarized XUV harmonics and linearly polarized IR component possesses the highest symmetry, i.e., axial symmetry with respect to the linear polarization vector. This geometry, as well as setup with crossed linearly polarized components, allows for the observation of RABBITT oscillations in both angle-integrated and angle-resolved probabilities of the electron emission.

On the contrary, for a circularly polarized IR field and either linearly or circularly polarized XUV comb (b), (d), only one symmetry plane exists, and RABBITT oscillations are observed only in the angular distribution of photoemission. In these geometries, the variation of the IR phase manifests in a rotation of the PAD with respect to the axis oriented along the direction of the IR component propagation.

To distinguish between the geometrical (inherited solely from the polarization of the electromagnetic field) and spectroscopic (inherited from the properties of the target, and thus dependent on photon energy) features, we considered neon and heliumlike targets. In the first case, the observable values are determined by the interplay between different ionization channels. In the second case, i.e., ionization of a s shell, for the systems (a) and (c) PAD does not depend on dynamic parameters, such as photon energy or even specific atom, and its form is determined only by polarization of the fields. For heliumlike system in the (b) geometry, the PAD reduces to partly geometrical with the incoherent part that does not depend on dynamical parameters, while the interference does depend.

For the circularly polarized XUV comb, the symmetries are the same for both multichannel targets and heliumlike ones. In the geometries with linearly polarized XUV component, there are two additional symmetry planes for heliumlike targets, moreover, for the linearly polarized IR component, they are geometrical and make angle $\pm\pi/4$ with polarization vector, while for the circularly polarized IR component, they are dynamical and depend on phase between absorption (up) and emission (down) transitions.

ACKNOWLEDGMENTS

The part of research related to the general approach (Sec. III) was funded by the Russian Science Foundation (RSF) under Project No. 22–12–00389 and the numerical simulations were supported by Ministry of Science and Higher Education of the Russian Federation Grant No. 075-15-2021-1353.

[1] *VUV and Soft X-Ray Photoionization*, edited by U. Becker and D. A. Shirley (Plenum, New York, 1996).

[2] F. J. Wuilleumier and M. Meyer, Pump-probe experiments in atoms involving laser and synchrotron radiation: an overview, J. Phys. B: At., Mol. Opt. Phys. **39**, R425 (2006).

[3] R. Mitzner, A. A. Sorokin, B. Siemer, S. Roling, M. Rutkowski, H. Zacharias, M. Neeb, T. Noll, F. Siewert, W. Eberhardt, M. Richter, P. Juranic, K. Tiedtke, and J. Feldhaus, Direct autocorrelation of soft-x-ray free-electron-laser pulses by time-resolved two-photon double ionization of he, Phys. Rev. A **80**, 025402 (2009).

[4] P. Radcliffe, S. Düterer, A. Azima, H. Redlin, J. Feldhaus, J. Dardis, K. Kavanagh, H. Luna, J. P. Gutierrez, P. Yeates, E. T. Kennedy, J. T. Costello, A. Delserieys, C. L. S. Lewis, R. Taïeb, A. Maquet, D. Cubaynes, and M. Meyer, Single-shot

characterization of independent femtosecond extreme ultraviolet free electron and infrared laser pulses, Appl. Phys. Lett. **90**, 131108 (2007).

[5] M. Lewenstein, P. Balcou, M. Y. Ivanov, A. L'Huillier, and P. B. Corkum, Theory of high-harmonic generation by low-frequency laser fields, Phys. Rev. A **49**, 2117 (1994).

[6] G. Sansone, E. Benedetti, F. Calegari, C. Vozzi, L. Avaldi, R. Flammini, L. Poletto, P. Villoresi, C. Altucci, R. Velotta, S. Stagira, S. D. Silvestri, and M. Nisoli, Isolated single-cycle attosecond pulses, Science **314**, 443 (2006).

[7] V. V. Strelkov, V. T. Platonenko, A. F. Sterzhantov, and M. Y. Ryabikin, Attosecond electromagnetic pulses: generation, measurement, and application. generation of high-order harmonics of an intense laser field for attosecond pulse production, Phys. Usp. **59**, 425 (2016).

[8] K. C. Prince, E. Allaria, C. Callegari, R. Cucini, G. D. Ninno, S. D. Mitri *et al.*, Coherent control with a short-wavelength free-electron laser, Nat. Photonics **10**, 176 (2016).

[9] C. Callegari, A. N. Grum-Grzhimailo, K. L. Ishikawa, K. C. Prince, G. Sansone, and K. Ueda, Atomic, molecular and optical physics applications of longitudinally coherent and narrow bandwidth free-electron lasers, Phys. Rep. **904**, 1 (2021), Atomic, molecular and optical physics applications of longitudinally coherent and narrow bandwidth Free-Electron Lasers.

[10] F. Krausz and M. Ivanov, Attosecond physics, Rev. Mod. Phys. **81**, 163 (2009).

[11] R. Pazourek, S. Nagele, and J. Burgdörfer, Time-resolved photoemission on the attosecond scale: opportunities and challenges, Faraday Discuss. **163**, 353 (2013).

[12] J. Vos, L. Cattaneo, S. Patchkovskii, T. Zimmermann, C. Cirelli, M. Lucchini, A. Kheifets, A. S. Landsman, and U. Keller, Orientation-dependent stereo wigner time delay and electron localization in a small molecule, Science **360**, 1326 (2018).

[13] M. Ossiander, J. Riemensberger, S. Neppl, M. Mittermair, M. Schäffer, A. Duensing, M. S. Wagner, R. Heider, M. Wurzer, M. Gerl *et al.*, Absolute timing of the photoelectric effect, Nature (London) **561**, 374 (2018).

[14] V. Véniard, R. Taïeb, and A. Maquet, Phase dependence of $(n+1)$-color $(n>1)$ ir-uv photoionization of atoms with higher harmonics, Phys. Rev. A **54**, 721 (1996).

[15] P. M. Paul, E. S. Toma, P. Breger, G. Mullot, F. Augé, P. Balcou, H. G. Muller, and P. Agostini, Observation of a train of attosecond pulses from high harmonic generation, Science **292**, 1689 (2001).

[16] H. Muller, Reconstruction of attosecond harmonic beating by interference of two-photon transitions, Appl. Phys. B **74**, s17 (2002).

[17] Y. Mairesse, A. de Bohan, L. J. Frasinski, H. Merdji, L. C. Dinu, P. Monchicourt, P. Breger, M. Kovaćev, R. Taïeb, B. Carrìe, H. G. Muller, P. Agostini, and P. Salières, Attosecond synchronization of high-harmonic soft x-rays, Science **302**, 1540 (2003).

[18] J. Dahlström, A. L'Huillier, and A. Maquet, Introduction to attosecond delays in photoionization, J. Phys. B: At., Mol. Opt. Phys. **45**, 183001 (2012).

[19] J. Dahlström, D. Guènot, K. Klünder, M. Gisselbrecht, J. Mauritsson, A. L'Huillier, A. Maquet, and R. Taïeb, Theory of attosecond delays in laser-assisted photoionization, Chem. Phys. **414**, 53 (2013).

[20] A. Harth, N. Douguet, K. Bartschat, R. Moshammer, and T. Pfeifer, Extracting phase information on continuum-continuum couplings, Phys. Rev. A **99**, 023410 (2019).

[21] A. S. Kheifets and A. W. Bray, RABBITT phase transition across the ionization threshold, Phys. Rev. A **103**, L011101 (2021).

[22] G. Laurent, W. Cao, H. Li, Z. Wang, I. Ben-Itzhak, and C. L. Cocke, Attosecond control of orbital parity mix interferences and the relative phase of even and odd harmonics in an attosecond pulse train, Phys. Rev. Lett. **109**, 083001 (2012).

[23] S. A. Aseyev, Y. Ni, L. J. Frasinski, H. G. Muller, and M. J. J. Vrakking, Attosecond angle-resolved photoelectron spectroscopy, Phys. Rev. Lett. **91**, 223902 (2003).

[24] D. Villeneuve, P. Hockett, M. Vrakking, and H. Niikura, Coherent imaging of an attosecond electron wave packet, Science **356**, 1150 (2017).

[25] J. Joseph, F. Holzmeier, D. Bresteau, C. Spezzani, T. Ruchon, J. F. Hergott, O. Tcherbakoff, P. D. Oliveira, J. C. Houver, and D. Dowek, Angle-resolved studies of XUV - IR two-photon ionization in the RABBITT scheme, J. Phys. B: At., Mol. Opt. Phys. **53**, 184007 (2020).

[26] C. Cirelli, C. Marante, S. Heuser, C. L. M. Petersson, Á. J. Galán, L. Argenti, S. Zhong, D. Busto, M. Isinger, S. Nandi *et al.*, Anisotropic photoemission time delays close to a fano resonance, Nat. Commun. **9**, 955 (2018).

[27] W. Jiang, G. S. J. Armstrong, J. Tong, Y. Xu, Z. Zuo, J. Qiang, P. Lu, D. D. A. Clarke, J. Benda, A. Fleischer *et al.*, Atomic partial wave meter by attosecond coincidence metrology, Nat. Commun. **13**, 5072 (2022).

[28] A. S. Kheifets and Z. Xu, Polarization control of RABBITT in noble gas atoms, J. Phys. B: At., Mol. Opt. Phys. **56**, 155601 (2023).

[29] S. Heuser, A. Jiménez Galán, C. Cirelli, C. Marante, M. Sabbar, R. Boge, M. Lucchini, L. Gallmann, I. Ivanov, A. S. Kheifets, J. M. Dahlström, E. Lindroth, L. Argenti, F. Martín, and U. Keller, Angular dependence of photoemission time delay in helium, Phys. Rev. A **94**, 063409 (2016).

[30] P. Hockett, Angle-resolved RABBITT: theory and numerics, J. Phys. B: At., Mol. Opt. Phys. **50**, 154002 (2017).

[31] D. Busto, J. Vinbladh, S. Zhong, M. Isinger, S. Nandi, S. Maclot, P. Johnsson, M. Gisselbrecht, A. L'Huillier, E. Lindroth, and J. M. Dahlström, Fano's propensity rule in angle-resolved attosecond pump-probe photoionization, Phys. Rev. Lett. **123**, 133201 (2019).

[32] J. Fuchs, N. Douguet, S. Donsa, F. Martin, J. Burgdörfer, L. Argenti, L. Cattaneo, and U. Keller, Time delays from one-photon transitions in the continuum, Optica **7**, 154 (2020).

[33] D. Bharti, H. Srinivas, F. Shobeiry, K. R. Hamilton, R. Moshammer, T. Pfeifer, K. Bartschat, and A. Harth, Multiside-band interference structures observed via high-order photon-induced continuum-continuum transitions in argon, Phys. Rev. A **107**, 022801 (2023).

[34] J. Peschel, D. Busto, M. Plach *et al.*, Attosecond dynamics of multi-channel single photon ionization, Nat. Commun. **13**, 5205 (2022).

[35] A. N. Grum-Grzhimailo, S. Fritzsche, P. O'Keeffe, and M. Meyer, Universal scaling of resonances in vector correlation photoionization parameters, J. Phys. B: At., Mol. Opt. Phys. **38**, 2545 (2005).

[36] M. Lucchini, L. Castiglioni, L. Kasmi, P. Kliuiev, A. Ludwig, M. Greif, J. Osterwalder, M. Hengsberger, L. Gallmann, and U. Keller, Light-matter interaction at surfaces in the spatiotemporal limit of macroscopic models, Phys. Rev. Lett. **115**, 137401 (2015).

[37] M. J. Ambrosio and U. Thumm, Electronic structure effects in spatiotemporally resolved photoemission interferograms of copper surfaces, Phys. Rev. A **96**, 051403(R) (2017).

[38] M. J. Ambrosio and U. Thumm, Spatiotemporal analysis of a final-state shape resonance in interferometric photoemission from Cu(111) surfaces, Phys. Rev. A **100**, 043412 (2019).

[39] P. K. Maroju, C. Grazioli, M. D. Fraia, M. Moioli, D. Ertel, H. Ahmadi, O. Plekan, P. Finetti, E. Allaria, L. Giannessi, G. D. Ninno, S. Spampinati, A. A. Lutman, R. J. Squibb, R. Feifel, P. Carpeggiani, M. Reduzzi, T. Mazza, M. Meyer, S. Bengtsson *et al.*, Attosecond pulse shaping using a seeded free-electron laser, Nature (London) **578**, 386 (2020).

[40] P. K. Maroju, C. Grazioli, M. D. Fraia, M. Moioli, D. Ertel, H. Ahmadi, O. Plekan, P. Finetti, E. Allaria, L. Giannessi, G. D. Ninno, S. Spampinati, A. A. Lutman, R. J. Squibb, R. Feifel, P. Carpeggiani, M. Reduzzi, T. Mazza, M. Meyer, S. Bengtsson *et al.*, Analysis of two-color photoelectron spectroscopy for attosecond metrology at seeded free-electron lasers, New J. Phys. **23**, 043046 (2021).

[41] P. K. Maroju, C. Grazioli, M. Di Fraia, M. Moioli, D. Ertel, H. Ahmadi, O. Plekan, P. Finetti, E. Allaria, L. Giannessi, G. De Ninno, A. A. Lutman, R. J. Squibb, R. Feifel, P. Carpeggiani, M. Reduzzi, T. Mazza, M. Meyer, S. Bengtsson, N. Ibrakovic *et al.*, Complex attosecond waveform synthesis at fel fermi, Appl. Sci. **11**, 9791 (2021).

[42] D. I. R. Boll and O. A. Fojón, Attosecond polarization control in atomic RABBITT-like experiments assisted by a circularly polarized laser, J. Phys. B: At., Mol. Opt. Phys. **50**, 235604 (2017).

[43] Y. Liao, E. Olofsson, J. M. Dahlström, L.-W. Pi, Y. Zhou, and P. Lu, Circularly polarized rabbitt applied to a rabi-cycling atom, Phys. Rev. A **109**, 043104 (2024).

[44] A. Fleischer, O. Kfir, T. Diskin, P. Sidorenko, and O. Cohen, Spin angular momentum and tunable polarization in high-harmonic generation, Nat. Photonics **8**, 543 (2014).

[45] M. Ivanov and E. Pisanty, Taking control of polarization, Nat. Photonics **8**, 501 (2014).

[46] M. Han, J. Ji, T. Balčiūnas *et al.*, Attosecond circular-dichroism chronoscopy of electron vortices, Nat. Phys. **19**, 1649 (2023).

[47] T. S. Sarantseva, A. A. Romanov, A. A. Silaev, N. V. Vvedenskii, and M. V. Frolov, High-order harmonic generation in orthogonal ir and xuv pulses: Xuv-initiated channel separation and polarization control, Phys. Rev. A **107**, 023113 (2023).

[48] M. Popova, S. Yudin, E. Gryzlova, M. Kiselev, and A. Grum-Grzhimailo, Attosecond interferometry involving discrete states, J. Exp. Theor. Phys. **136**, 259 (2023).

[49] S. Yudin, M. Popova, M. Kiselev, S. Burkov, E. Gryzlova, and A. Grum-Grzhimailo, Attosecond interferometry of neon atom: Photoelectron angular distributions, Moscow Univ. Phys. Bulletin **78**, 347 (2023).

[50] L. A. Nikolopoulos, Amplitude coefficient equations, *Elements of Photoionization Quantum Dynamics Methods* (Institute of Physics Publishing, Bristol, 2019).

[51] C. Froese Fischer, T. Brage, and P. Jönsson, *Computational Atomic Structure. An MCHF Approach* (Institute of Physics Publishing, Bristol, 1997).

[52] T. Mercouris, Y. Komninos, S. Dionissopoulou, and C. A. Nicolaides, Effects on observables of the singularity in the multiphoton free - free dipole matrix elements, J. Phys. B: At., Mol. Opt. Phys. **29**, L13 (1996).